

# Quantum-Electron Back Action on Hybridization of Radiative and Evanescent Field Modes

Andrii Iurov<sup>1</sup>, Danhong Huang<sup>2</sup>, Godfrey Gumbs<sup>3</sup>, Wei Pan<sup>4</sup> and A. A. Maradudin<sup>5</sup>

<sup>1</sup>*Center for High Technology Materials,  
University of New Mexico, 1313 Goddard SE,  
Albuquerque, New Mexico, 87106, USA*

<sup>2</sup>*Air Force Research Laboratory, Space Vehicles Directorate,  
Kirtland Air Force Base, New Mexico 87117, USA*

<sup>3</sup>*Department of Physics and Astronomy,  
Hunter College of the City University of New York,  
695 Park Avenue New York, New York 10065, USA*

<sup>4</sup>*Sandia National Laboratories, Albuquerque, New Mexico 87185, USA*

<sup>5</sup>*Department of Physics and Astronomy,  
University of California, Irvine, California 92697, USA*

(Dated: November 11, 2021)

## Abstract

A back action from Dirac electrons in graphene on the hybridization of radiative and evanescent fields is found as an analogy to Newton's third law. Here, the back action appears as a localized polarization field which greatly modifies an incident surface-plasmon-polariton (SPP) field. This yields a high sensitivity to local dielectric environments and provides a scrutiny tool for molecules or proteins selectively bounded with carbons. A scattering matrix is shown with varied frequencies nearby the surface-plasmon (SP) resonance for the increase, decrease and even a full suppression of the polarization field, which enables accurate effective-medium theories to be constructed for Maxwell-equation finite-difference time-domain methods. Moreover, double peaks in the absorption spectra for hybrid SP and graphene-plasmon modes are significant only with a large conductor plasma frequency, but are overshadowed by a round SPP peak at a small plasma frequency as the graphene is placed close to conductor surface. These resonant absorptions facilitate the polariton-only excitations, leading to polariton condensation for a threshold-free laser.

*Introduction:* “For every action, there is an equal and opposite reaction.” as famously stated by the Newton’s third law in classical mechanics. It is known that when light is incident on a semiconductor, its energetic photons can lift electrons from a lower valence band to a higher conduction band, leaving many electron-hole pairs in the system<sup>1,2</sup>. Simultaneously, its electric-field component will further push away these negatively (positively) charged electrons (holes) in opposite field directions. For this instance, however, *do excited electrons and holes exert an action back on the incident light?* The answer to this question lies in the induced optical-polarization field as a collection of local dipole moments from many displaced electrons and holes<sup>3,4</sup>, which plays a role in scattering the electric-field component of the incident light<sup>5,6</sup>. Therefore, the quantum nature of Dirac electrons<sup>7-10</sup> is expected to be reflected in this electron back action on the incident light with a complex distribution of Landau-damping regions in comparison with that of two-dimensional electron gases in a quantum well.

For a hybrid system illustrated in Fig. 1a, we encounter radiative field modes, such as photons and polaritons<sup>11-15</sup>, as well as evanescent field modes, e.g., surface and graphene plasmons<sup>16-18</sup>. Researches on optical responses of graphene electrons have been reported before<sup>18,19</sup>, but most of those efforts are limited to the radiation or grating-deflection field coupling. In contrast to the plane-wave-like external field, we explore the surface-plasmon-polariton near-field<sup>20-22</sup> coupling to graphene electrons with a different dispersion relation from the usual linear one, i.e.,  $\omega = qc$ , for the free-space light. In our case, the graphene sheet is brought very close to the surface of a conducting substrate so that the hybridization of radiative and evanescent fields can occur<sup>23</sup>. As a result, the non-dispersive surface-plasmon mode is able to hybridize successively with radiative photon and polariton modes<sup>11,12</sup>, as well as with the spatially-localized graphene plasmon mode<sup>24</sup>, as shown schematically in Fig. 1b.

Such a distinctive dispersion relation of the hybrid quantum-plasmon modes should be experimentally observable in optical spectra<sup>25-28</sup>. The effective scattering matrix<sup>29,30</sup> from such a coupled system is found significantly different from either the graphene sheet or the conductor and it displays distinctive features from the retarded longitudinal Coulomb interaction<sup>6</sup> between electrons in the graphene sheet and conductor. This scattering matrix can be employed for constructing an effective-medium theory<sup>31-34</sup> to study the optical properties

of inserted biomolecules and metamaterials between the graphene sheets and the conductor surface. Therefore, a locally environment-sensitive super-resolution near-field imaging can be developed for functionalized biomolecules bounded with metallic nanodots and nanorods or even carbon atoms of graphene<sup>35</sup>.

Theory and Methods: As illustrated in Fig. 1a, our model system consists a thick conductor and a dielectric-embedded graphene sheet above its surface. A surface-plasmon-polariton field (SPPF) can be excited by incident light on a surface grating. This surface-propagating SPPF couples to Dirac electrons in graphene, and the induced polarization field from graphene acts back simultaneously on the SPPF as a resonant scatter.

Using the Green's function approach,<sup>5</sup> we convert Maxwell's equation for the electric field  $\mathbf{E}(\mathbf{r}, \omega)$  into an integral equation in the spatial ( $\mathbf{r}$ ) domain, including a nonlocal source term to scatter the incident SPPF  $\mathcal{E}^{\text{inc}}(\mathbf{r}, \omega)$ , where  $\omega$  is the light frequency. After a Fourier transform of this integral equation with respect to  $\mathbf{r}_{\parallel}$ , we obtain ( $\mu, \nu = 1, 2, 3$ )

$$E_{\mu}(\mathbf{q}_{\parallel}, \omega|x_3) = \mathcal{E}_{\mu}^{\text{inc}}(\mathbf{q}_{\parallel}, \omega|x_3) + \frac{\omega^2}{\epsilon_0 c^2} \sum_{\nu} g_{\mu\nu}(\mathbf{q}_{\parallel}, \omega|x_3, z_0) \mathcal{P}_{\nu}^{\text{s}}(\mathbf{q}_{\parallel}, \omega), \quad (1)$$

where  $\mathbf{r} = \{\mathbf{r}_{\parallel}, x_3\}$ ,  $x_3 = z_0$  denotes the graphene-sheet position, and  $g_{\mu\nu}(\mathbf{q}_{\parallel}, \omega|x_3, z_0)$  is the Fourier transformed Green's function matrix<sup>6</sup> which corresponds to a retarded coupling between graphene electrons to the incident SPPF. Based on linear-response theory<sup>36</sup>, we find the graphene polarization field in Eq. (1)  $\mathcal{P}_{\nu}^{\text{s}}(\mathbf{q}_{\parallel}, \omega) = \epsilon_0 \chi_{\text{s}}^{(0)}(q_{\parallel}, \omega) (1 - \delta_{\nu 3}) E_{\nu}(\mathbf{q}_{\parallel}, \omega|z_0)$ , where  $\chi_{\text{s}}^{(0)}(q_{\parallel}, \omega) = e^2 \Pi_{\text{s}}^{(0)}(q_{\parallel}, \omega) / [\epsilon_0 (q_{\parallel}^2 - \epsilon_{\text{d}} \omega^2 / c^2)]$  represents the optical-response function<sup>37</sup>, and  $\Pi_{\text{s}}^{(0)}(q_{\parallel}, \omega)$  is the density-density correlation function of graphene electrons<sup>38</sup>. Setting  $x_3 = z_0$  in Eq. (1), we obtain a self-consistent equation for  $\mathbf{E}(\mathbf{q}_{\parallel}, \omega|z_0)$ . Furthermore, if  $\mathcal{E}^{\text{inc}}(\mathbf{q}_{\parallel}, \omega|z_0) = 0$  is assumed in this self-consistent equation, we get the dispersion equation for the hybrid plasmon modes, and the resulting dispersion relation  $\omega = \Omega(\mathbf{q}_{\parallel}|z_0)$ , as illustrated in Fig. 1b, is determined from the real part of the secular equation  $\mathcal{D}et\{\vec{\mathcal{C}}(\mathbf{q}_{\parallel}, \omega|z_0)\} = 0$ , where  $\vec{\mathcal{C}}(\mathbf{q}_{\parallel}, \omega|z_0) = \delta_{\mu\nu} - (\omega/c)^2 g_{\mu\nu}(\mathbf{q}_{\parallel}, \omega|z_0, z_0) (1 - \delta_{\nu 3}) \chi_{\text{s}}^{(0)}(q_{\parallel}, \omega)$  is the complex coefficient matrix. After calculating the inverse of  $\vec{\mathcal{C}}$ ,  $\mathbf{E}(\mathbf{r}_{\parallel}, \omega|x_3)$  can be expressed explicitly as

$$E_{\mu}(\mathbf{r}_{\parallel}, \omega|x_3) = \mathcal{E}_{\mu}^{\text{inc}}(\mathbf{r}_{\parallel}, \omega|x_3) + \frac{\omega^2}{c^2} \int \frac{d^2 \mathbf{q}_{\parallel}}{(2\pi)^2} e^{i\mathbf{q}_{\parallel} \cdot \mathbf{r}_{\parallel}} \chi_{\text{s}}^{(0)}(q_{\parallel}, \omega)$$

$$\times \sum_{\nu} \left\{ g_{\mu\nu}(\mathbf{q}_{\parallel}, \omega | x_3, z_0) (1 - \delta_{\nu 3}) \left[ \sum_{\mu'} \mathcal{C}_{\nu\mu'}^{-1}(\mathbf{q}_{\parallel}, \omega | z_0) \mathcal{E}_{\mu'}^{\text{inc}}(\mathbf{q}_{\parallel}, \omega | z_0) \right] \right\}. \quad (2)$$

From Eq. (2) the Fourier transformed scattering matrix<sup>29</sup> is easily found to be

$$\alpha_{\mu\nu}^{\text{eff}}(\mathbf{q}_{\parallel}, \omega | x_3) = \frac{\omega^2}{c^2} \chi_s^{(0)}(q_{\parallel}, \omega) \sum_{\nu'} g_{\mu\nu'}(\mathbf{q}_{\parallel}, \omega | x_3, z_0) (1 - \delta_{\nu' 3}) \mathcal{C}_{\nu'\nu}^{-1}(\mathbf{q}_{\parallel}, \omega | z_0). \quad (3)$$

Additionally, by using the calculated  $\mathbf{E}(\mathbf{r}_{\parallel}, \omega | z_0)$  in Eq. (2), the absorption coefficient  $\beta_{\text{abs}}(\omega | z_0)$  for the SPPF can be calculated<sup>20,39</sup> based on the Lorentz function  $\alpha_L(\omega | z_0)$  given by

$$\alpha_L(\omega | z_0) = \frac{c}{\omega} \left| \sum_{\mu, \nu} \hat{e}_{\mu} \mathcal{C}_{\mu\nu}^{-1}(\mathbf{k}_0, \omega | z_0) \left[ i\hat{k}_{\nu} \beta_3(\omega) - \hat{x}_{\nu} k_0(\omega) \right] e^{-\beta_3(\omega) z_0} \right| \\ \times \left( \frac{2\pi e^2}{\epsilon_0 \epsilon_r k_0} \right) \sqrt{1 - \frac{\epsilon_d \omega^2}{k_0^2 c^2}} \left\{ \Pi_s^{(0)}(k_0, \omega) + [\Pi_s^{(0)}(k_0, -\omega)]^* \right\}, \quad (4)$$

where  $\epsilon_r$  is the graphene dielectric constant,  $\hat{e}$  and  $\hat{\mathbf{k}}$  are the unit polarization and wave vectors of the SPPF,  $\hat{\mathbf{x}} = (0, 0, 1)$  is the spatial unit vector,  $\mathbf{k}_0 \equiv \text{Re}[k_0(\omega)]\hat{\mathbf{k}}$ ,  $\beta_3(\omega) = \sqrt{k_0^2(\omega) - \omega^2/c^2}$ ,  $k_0(\omega) = (\omega/c)\sqrt{\epsilon_d \epsilon_c(\omega)/[\epsilon_d + \epsilon_c(\omega)]}$ ,  $\epsilon_d$  is the cladding-layer dielectric constant, and  $\epsilon_c(\omega) = \epsilon_s - \Omega_p^2/\omega^2$  for the conductor.

*Results and Discussions:* In our numerical calculations, we use the Fermi wave vector  $k_F = \sqrt{\pi n_0}$  as the scale for wave numbers,  $1/k_F$  for lengths, and  $E_F = \hbar v_F k_F$  for energies. The direction of SPPF propagation is chosen  $\hat{\mathbf{k}} = (1, 0, 0)$  for simplicity, and we also set  $\epsilon_s = 13.3$ ,  $\epsilon_d = \epsilon_r = 2.4$ ,  $v_F = 1 \times 10^8$  cm/s, and  $n_0 = 5 \times 10^{11}$  cm<sup>-2</sup> for the doping density in graphene. Moreover, the half gap  $\Delta = 0$  is assumed unless it is stated in figure captions, and the resonant frequency  $\Omega_r = \Omega_p/\sqrt{\epsilon_s + \epsilon_d}$  will be given directly in figure captions.

For a retarded interaction between light and graphene electrons, both radiative and evanescent modes must be considered in the hybrid system. The radiative modes include photons and polaritons, while the evanescent modes appear as surface-plasmon polaritons (SPPs), graphene plasmons (G-Ps), and surface plasmons (SPs). Figure 2 displays the real part of  $\mathcal{D}^{-1}(q_x, \omega | z_0) \equiv 1/\mathcal{D}et[\vec{\mathcal{C}}(q_x, \omega | z_0)]$  for four different  $q_x$  ranges. As seen from Fig. 2a, in addition to the SPP mode, the hybridizations of both radiative photon and polariton modes with localized SPs (labeled by  $q_1$  and  $q_2$  in Fig. 1b) show up in this very small  $q_x$  range. As the  $q_x$  range slightly expands in Fig. 2b, the SPP mode in Fig. 2a is fully developed, which is accompanied by a G-P mode at very low energies. As the  $q_x$  range further

increases in Figs. 2c and 2d, the G-P energy exceeds that of the SP. Consequently, the anticrossing of G-Ps with SPPs (labeled by  $q_3$  in Fig. 1b) shows up.

The  $z_0$  dependence in the secular equation reflects the distinctive evanescent coupling between SPPs and G-Ps. Here, the factor  $g_{\mu\nu}(q_x, \omega|z_0, z_0)$  plays the role of a retarded SPP coupling to a spatially-separated G-P, while  $\chi_s^{(0)}(q_x, \omega)$  corresponds to the G-P optical response. Therefore, their product represents the hybrid Dirac-SPP modes. By moving the graphene sheet a bit further from the conductor surface in Fig. 3, the anticrossing gap shrinks due to decreased retarded coupling. Simultaneously, the strengths of all the plasmon, polariton and photon modes increase by more than one order of magnitude due to loss suppression of these modes to the conductor.

The incident SPPF suffers not only Ohmic loss during its propagation along the conductor surface, but also absorption loss by its coupling to G-Ps. Figure 4 presents the absorption spectra  $\beta_{\text{abs}}(\omega|z_0)$  with various  $\Delta$  in (a) and different  $z_0$  in (b). From Fig. 4a we find three absorption peaks for  $\Delta = 0$ , where two sharp ones correspond to G-Ps (right) and SPs (left), as seen from Figs. 2c and 2d, with a deep dip between them for the opened anticrossing gap labeled by  $q_3$  in Fig. 1b. The lowest round peak is for SPP modes, as shown in Figs. 2a and 2b, which is separated from the SP peak by a shallow dip labeled by  $q_2$  in Fig. 1b. An absorption spike also shows up on the shoulder of this round peak for  $\Delta > 0$  and it shifts to higher energy with increasing  $\Delta$ . The spike feature for  $\Delta > 0$  is rooted in the light-frequency dependence in  $k_0(\omega)$  for unique evanescent coupling and is a result of  $\Delta$  driven modification in suppressing the Landau damping<sup>38</sup>, i.e. the  $\text{Im}[\Pi_s^{(0)}(k_0, \omega)]$  term in Eq. (4), for very large  $k_0$  values with increasing  $\omega$  towards  $\Omega_r$ . The absorption peak from the indistinguishable SPP and SP modes increases greatly in the inset of Fig. 4a for a lower SP resonance  $\hbar\Omega_r/E_F = 0.25$  since the SPPF decay is largely eased at a much smaller  $q_x$ . The enhancement of the SPP absorption peak is also seen in Fig. 4b for small  $z_0$  due to reduced SPPF decay. Additionally, we find from the inset of Fig. 4b that the decrease of  $\beta_{\text{abs}}(\omega|z_0)$  with increasing  $z_0$  becomes much more dramatic as  $\omega$  approaches  $\Omega_r$  with increased SPPF localization.

In addition to the SPPF optical absorption by G-Ps, a resonant scattering of the SPPF from G-Ps also happens, as described by Eq. (3). Figure 5 presents 3D plots for  $[\text{Re}\{\alpha_{11}^{\text{eff}}(q_x, \omega|x_3)\}]^{1/5}$  with four  $\omega$  values, where the graphene sheet is put relatively close to

the surface. Here, the scattering matrix is  $\alpha_{\mu\nu}^{\text{eff}} \equiv \delta(E_\mu - \mathcal{E}_\mu^{\text{inc}})/\delta\mathcal{E}_\nu^{\text{inc}}$ , and its signs correspond to enhanced (+) or weakened (-) SPPF after light scattering with G-Ps. If both  $q_x$  and  $x_3$  are large, such scattering is largely suppressed, leaving only a large and flat basin in the upper-right corners of Figs. 5a-5d. If  $q_x$  is very small, the photon and SPP radiative modes dominate, and then,  $\text{Re}\{\alpha_{11}^{\text{eff}}(q_x, \omega|x_3)\}$  remains negative and becomes independent of  $x_3$ . When  $q_x$  is intermediate, the SPP evanescent modes start entering in with increasing  $\omega$  up to  $\Omega_r$ . In this case, the positive-peak strength reduces and the peak coverage is squeezed into a smaller  $x_3$  region where the localization of SPPF is still insignificant. In addition, the positive peak splits into two islands at  $\omega = 0.9\Omega_r$  and eventually switches to a negative peak followed by a negative constant at  $\omega = \Omega_r$ . On the other hand, when  $q_x$  becomes very large for a strongly-localized SPPF, its scattering by G-P becomes negligible except for the region very close to the surface as shown by the sharp negative edges in the lower-right corners of Figs. 5a-5d.

By moving the graphene sheet so it becomes well separated from the conductor surface, as shown in Fig. 6, we expect the scattering effects from G-Ps on the SPPF to be limited to a narrow area surrounding the graphene sheet for large  $q_x$  values. Indeed, when  $q_x$  is large, we find  $\text{Re}\{\alpha_{11}^{\text{eff}}(q_x, \omega|x_3)\} = 0$  for  $x_3$  far away from the graphene sheet at  $z_0$  in the upper- and lower-right corners of Figs. 6a-6d. For small  $q_x$  values, however, the positive peak appears, as in Fig. 5, and its coverage crawls out along  $x_3 = z_0$  to a relative large  $q_x$  region followed by a negative sharp edge, although its peak strength decreases with increasing  $\omega$  towards  $\Omega_r$ . This extended region becomes separated from the positive peak at  $\omega = 0.9\Omega_r$  in Fig. 6c to form an island, and both the positive peak and island disappear and are eventually replaced by negative sharp and stepped edges at  $\omega = \Omega_r$  in Fig. 6d.

*Summary:* An analogy to Newton's third law in classical mechanics has been demonstrated by the effect of electron back action on the hybridization of radiative and evanescent fields using a retarded interaction, which is seen as the hybrid dispersions for both radiative (small  $q_x$  range) and evanescent (large  $q_x$  range) field modes. Instead of a reaction force, the back action in this study is an induced optical-polarization field from the Dirac plasmons, which resonantly redistributes an incident surface-plasmon-polariton field by scattering. The localization characteristics of such a retarded interaction ensures a very high sensitivity to dielectric environments surrounding the graphene, including variations in the conducting

substrate, cladding layer, electronic properties of embedded graphene, as well as the graphene distance from the conductor surface. This provides a unique advantage in wavelength-sensitive optical scrutinizing for chemically-active molecules or proteins bounded with carbon atoms in graphene.

The optical probing tools discussed in this study include either scattering or optical absorption of an incident electromagnetic field. For light scattering, we calculate the spatial-temporal dependence of a Fourier transformed scattering matrix, which clearly displays the scattering enhancement, weakening and even suppression as functions of both graphene separations ( $z_0$ ) from the conductor surface and wave numbers ( $q_x$ ) of the evanescent surface-plasmon-polariton field at several frequencies close to the localized surface-plasmon resonance. This derived scattering matrix lays the foundation for constructing an effective-medium theory commonly employed in finite-difference time-domain methods<sup>40</sup> for solving Maxwell's equations. For field absorption, the double peaks associated with hybrid surface and graphene plasmon modes at the high-energy side are shown to be dominant for high conductor plasma frequencies. However, the round peak at the low-energy side takes the dominant role at low plasma frequencies. Additionally, this round peak shows that localized modes can be greatly enhanced when the graphene is moved close to the conductor surface. These unique features in resonant absorption enable the selective excitation of radiative polariton modes for their condensation and a threshold-free laser afterwards.

Acknowledgments: D.H. would like to thank the support from the Air Force Office of Scientific Research (AFOSR).

---

<sup>1</sup> H. Haug and S. W. Koch, *Quantum Theory of the Optical and Electronic Properties of Semiconductors* (Fourth Edition, World Scientific Publishing Co. Pte. Ltd., 2004).

<sup>2</sup> F. Rossi and T. Kuhn, *Rev. Mod. Phys.* **74**, 895 (2002).

<sup>3</sup> M. Lindberg and S. W. Koch, *Phys. Rev. B* **38**, 3342 (1988).

<sup>4</sup> M. Kira and S. W. Koch, *Progress in Quantum Electronics* **30**, 155 (2006).

<sup>5</sup> D. H. Huang, M. M. Easter, G. Gumbs, A. A. Maradudin, S.-Y. Lin, D. A. Cardimona and X. Zhang, *Opt. Expr.* **22**, 27576 (2014).

<sup>6</sup> D. H. Huang, M. M. Easter, G. Gumbs, A. A. Maradudin, S.-Y. Lin, D. A. Cardimona, and X.

- Zhang, Appl. Phys. Lett. **104**, 251103 (2014).
- <sup>7</sup> K. Novoselov, A. K. Geim, S. Morozov, D. Jiang, M. Katsnelson, I. Grigorieva, S. Dubonos, and A. Firsov, Nature **438**, 197 (2005).
- <sup>8</sup> A. K. Geim and K. S. Novoselov, Nature Materials **6**, 183 (2007).
- <sup>9</sup> Y. Zhang, Y.-W. Tan, H. L. Störmer, and P. Kim, Nature **438**, 201 (2005).
- <sup>10</sup> A. K. Geim, Science **324**, 1530 (2009).
- <sup>11</sup> S. Christopoulos, G. B. H. von Högersthal, A. J. D. Grundy, P. G. Lagoudakis, A.V. Kavokin, J. J. Baumberg, G. Christmann, R. Butté, E. Feltin, J.-F. Carlin, and N. Grandjean, Phys. Rev. Lett. **98**, 126405 (2007).
- <sup>12</sup> S. I. Tsintzos, N. T. Pelekanos, G. Konstantinidis, Z. Hatzopoulos, and P. G. Savvidis, Nat. Lett. **453**, 372 (2008).
- <sup>13</sup> P. Bhattacharya, B. Xiao, A. Das, S. Bhowmick, and J. Heo, Phys. Rev. Lett. **110**, 206403 (2013).
- <sup>14</sup> C. Schneider, A. Rahimi-Iman, N. Y. Kim, J. Fischer, I. G. Savenko, M. Amthor, M. Lermer, A. Wolf, L. Worschech, V. D. Kulakovskii, I. A. Shelykh, M. Kamp, S. Reitzenstein, A. Forchel, Y. Yamamoto, and S. Höfling, Nat. **497**, 348 (2013).
- <sup>15</sup> E. L. Albuquerque and M. G. Cottam, Phys. Rep. **233**, 67 (1993).
- <sup>16</sup> B. Wang, X. Zhang, F. J. García-Vidal, X. Yuan, and J. Teng, Phys. Rev. Lett. **109**, 073901 (2012).
- <sup>17</sup> M. Liu, X. Yin, and X. Zhang, Nano Letters **12**, 1482 (2012).
- <sup>18</sup> M. Liu, X. Yin, E. Ulin-Avila, B. Geng, T. Zentgraf, L. Ju, F. Wang, and X. Zhang, Nature **474**, 64 (2011).
- <sup>19</sup> F. Koppens, T. Mueller, P. Avouris, A. Ferrari, M. Vitiello, and M. Polini, Nature nanotechnology **9**, 780 (2014).
- <sup>20</sup> A. A. Maradudin and D. L. Mills, Phys. Rev. B **11**, 1392 (1975).
- <sup>21</sup> M. G. Cottam and A. A. Maradudin, “Surface linear response functions”, in *Surface Excitations*, eds. V. M. Agranovich and R. Loudon (North-Holland, Amsterdam, 1984), pp. 1-194.
- <sup>22</sup> J. M. Pitarke, V. M. Silkin, E. V. Chulkov, and P. M. Echenique, Rep. Prog. Phys. **70**, 1 (2007).
- <sup>23</sup> A. V. Zayats, I. I. Smolyaninov, and A. A. Maradudin, Phys. Rep. **408**, 131 (2005).
- <sup>24</sup> A. Iurov, G. Gumbs, D. Huang, and V. Silkin, Phys. Rev. B **93**, 035404 (2016).
- <sup>25</sup> M. S. Tame, K. R. McEnery, S. K. Özdemir, J. Lee, S. A. Maier, and M. S. Kim, Nat. Phys. **9**,

- 329 (2013).
- <sup>26</sup> F. de León-Pérez, G. Brucoli, F. J. Garca-Vidal, and L. Martín-Moreno, *New J. Phys.* **10**, 105017 (2008).
- <sup>27</sup> A. N. Grigorenko, M. Polini, and K. S. Novoselov, *Nature Photonics* **6**, 749 (2012).
- <sup>28</sup> D. N. Basov, M. M. Fogler, A. Lanzara, F. Wang Y. Zhang, *Rev. Mod. Phys.* **86**, 959 (2014).
- <sup>29</sup> D. S. Saxon, *Phys. Rev.* **100**, 1771 (1955).
- <sup>30</sup> F. J. García de Abajo, *Rev. Mod. Phys.* **79**, 1267 (2007).
- <sup>31</sup> J. van Kranendonk and J. E. Sipe, “Foundations of the macroscopic electromagnetic theory of dielectric media”, in *Progress in Optics XV*, ed. E. Wolf (New York: North-Holland, 1977), Chap. 5.
- <sup>32</sup> G. D. Mahan and G. Obermair, *Phys. Rev.* **183**, 834 (1969).
- <sup>33</sup> J. Sipe and J. van Kranendonk, *Phys. Rev. A* **9**, 1806 (1974).
- <sup>34</sup> W. Lamb, D. M. Wood, N. W. Ashcroft, *Phys. Rev. B* **21**, 2248 (1980).
- <sup>35</sup> M. Wojcik, M. Hauser, W. Li, S. Moon, and K. Xu, *Nature Communications* **6**, 7384 (2015).
- <sup>36</sup> G. Gumbs and D. H. Huang, *Properties of Interacting Low-Dimensional Systems* (John Wiley & Sons, 2011), Chap. 2.
- <sup>37</sup> D. H. Huang, G. Gumbs and O. Roslyak, *Applied Optics* **52**, 755 (2013).
- <sup>38</sup> O. Roslyak, G. Gumbs and D. H. Huang, *J. Appl. Phys.* **109**, 113721 (2011).
- <sup>39</sup> D. H. Huang and Y. Zhao, *Physical Review A* **51**, 1617 (1995).
- <sup>40</sup> A. F. Oskooi, D. Roundy, M. Ibanescu, P. Bermel, J. D. Joannopoulos, S. G. Johnson, *Computer Physics Communications* **181**, 687 (2010).

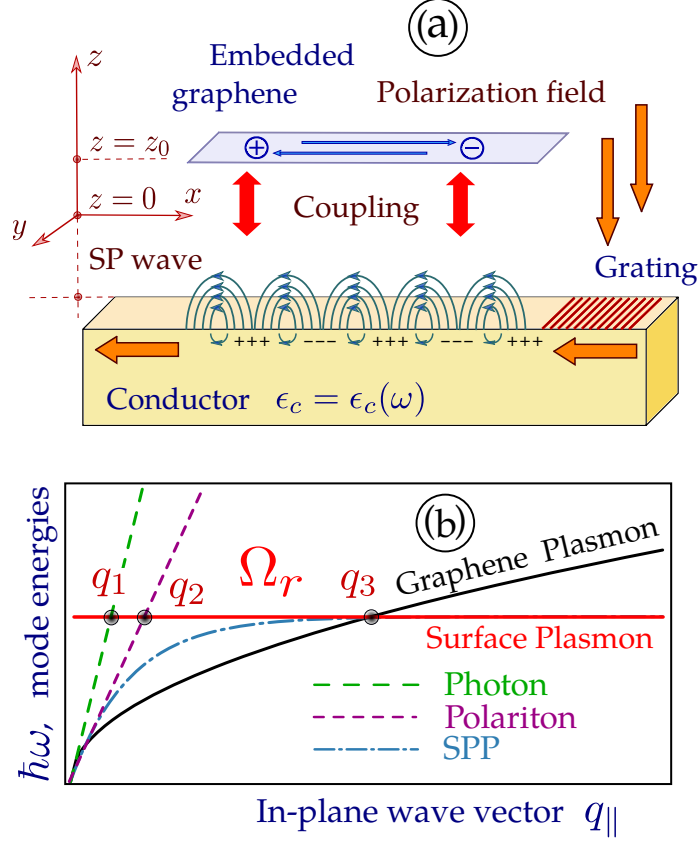


FIG. 1. Schematic (a) for a thick conductor  $\epsilon_c(\omega)$  and an embedded graphene sheet at  $z = z_0$  above its surface at  $z = 0$  within a cladding dielectric  $\epsilon_d$ . The surface-plasmon-polariton field (SPPF) is excited by light incident on a grating. The propagating SPPF excites Dirac electrons in graphene, and the induced graphene polarization modifies the SPPF by resonant scattering. Illustration (b) for energy dispersions of photons, polaritons, surface-plasmon polaritons (SPPs), graphene plasmons (G-Ps) and surface plasmons (SPs), where three labeled circles indicate the mode hybridizations.

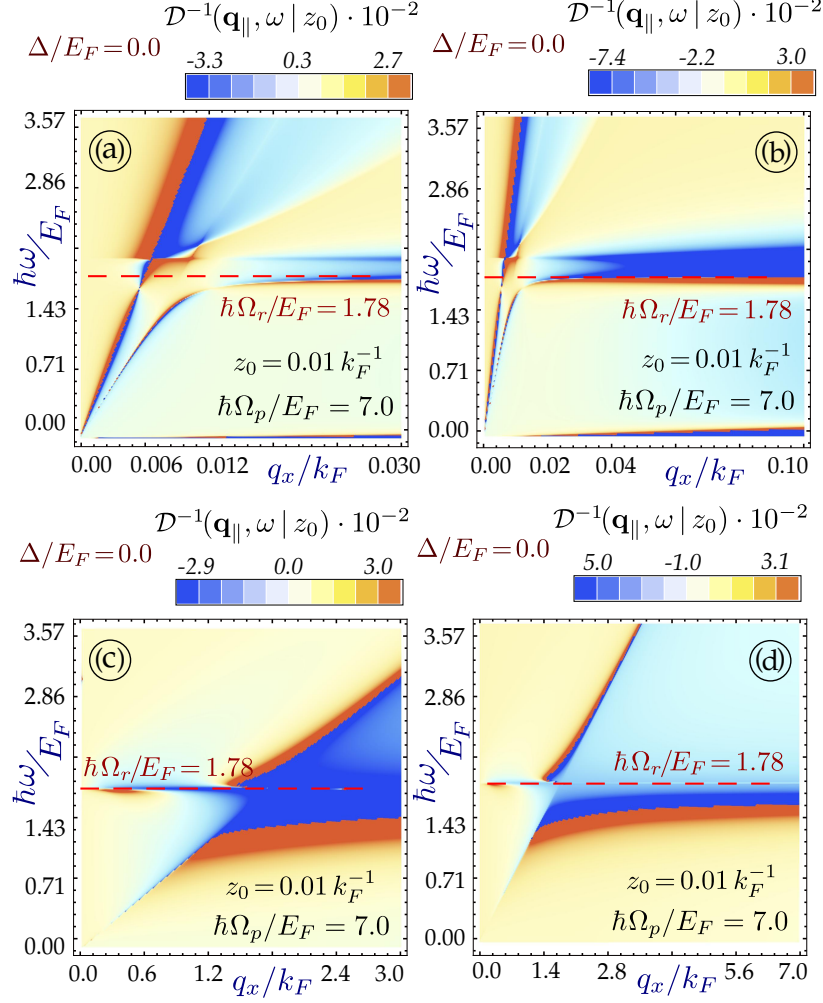


FIG. 2. Density plots for the real part of  $\mathcal{D}^{-1}(q_x, \omega | z_0) \equiv 1/\mathcal{D}et\{\overset{\leftrightarrow}{\mathcal{C}}(q_x, \omega | z_0)\}$  in four different  $q_x$  ranges growing from 0.03 to 7 with hybrid-plasmon dispersions indicated by jumps between positive (red) and negative (blue) peaks. Here,  $k_F z_0 = 0.01$ ,  $\hbar\Omega_r/E_F = 1.78$ .

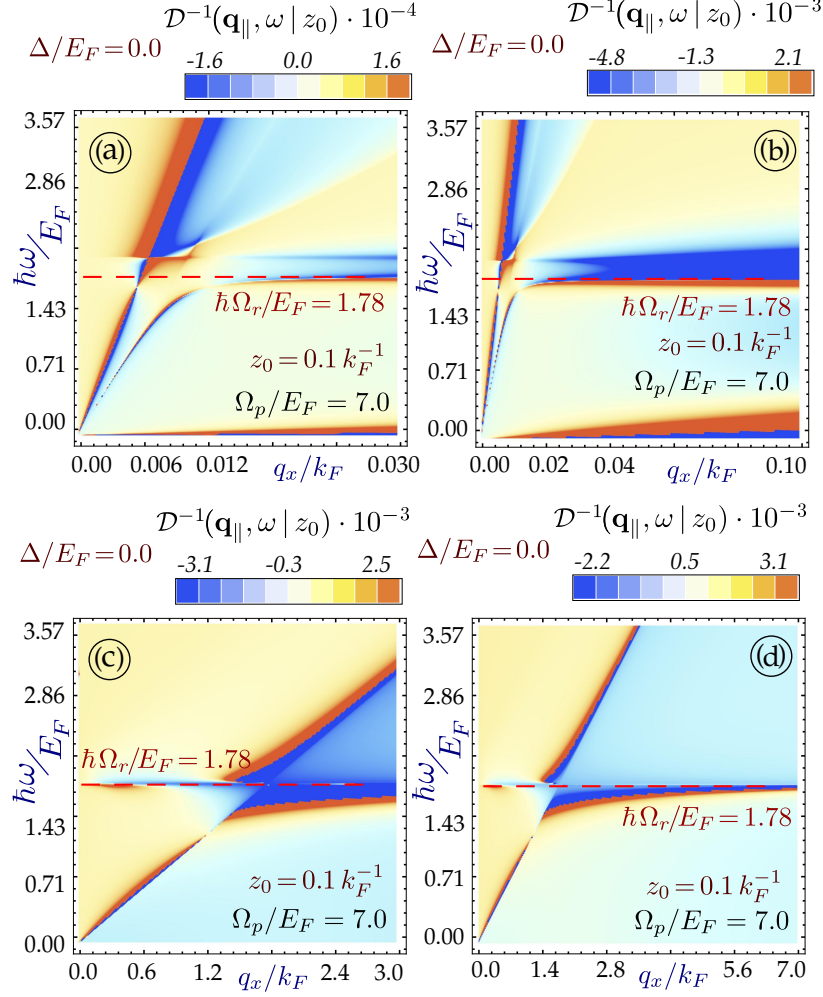


FIG. 3. Density plots for the real part of  $\mathcal{D}^{-1}(q_x, \omega | z_0)$  for four different  $q_x$  ranges growing from 0.03 to 7. Here,  $k_F z_0 = 0.1$ ,  $\hbar\Omega_r/E_F = 1.78$ .

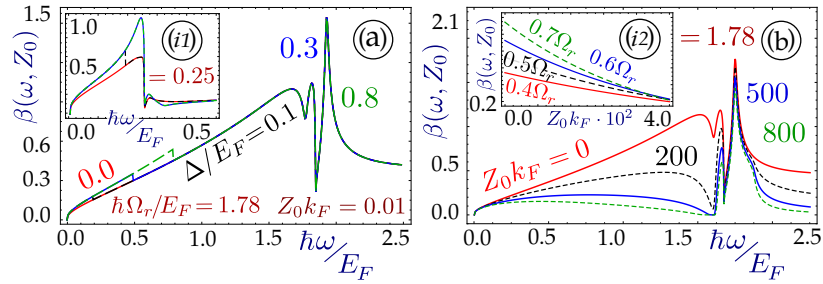


FIG. 4. Absorption spectra  $\beta_{\text{abs}}(\omega | z_0)$  displayed in (a) with  $k_F z_0 = 0.01$  for  $\Delta/E_F = 0, 0.1, 0.3, 0.8$ , where  $\hbar\Omega_r/E_F = 1.78$  and 0.25 in its inset. In (b),  $\beta_{\text{abs}}(\omega | z_0)$  with  $\hbar\Omega_r/E_F = 1.78$ ,  $\Delta/E_F = 0$  for  $k_F z_0 = 0, 200, 500, 800$ , and its  $z_0$  dependence in the inset for  $\omega/\Omega_r = 0.4, 0.5, 0.6, 0.7$ .

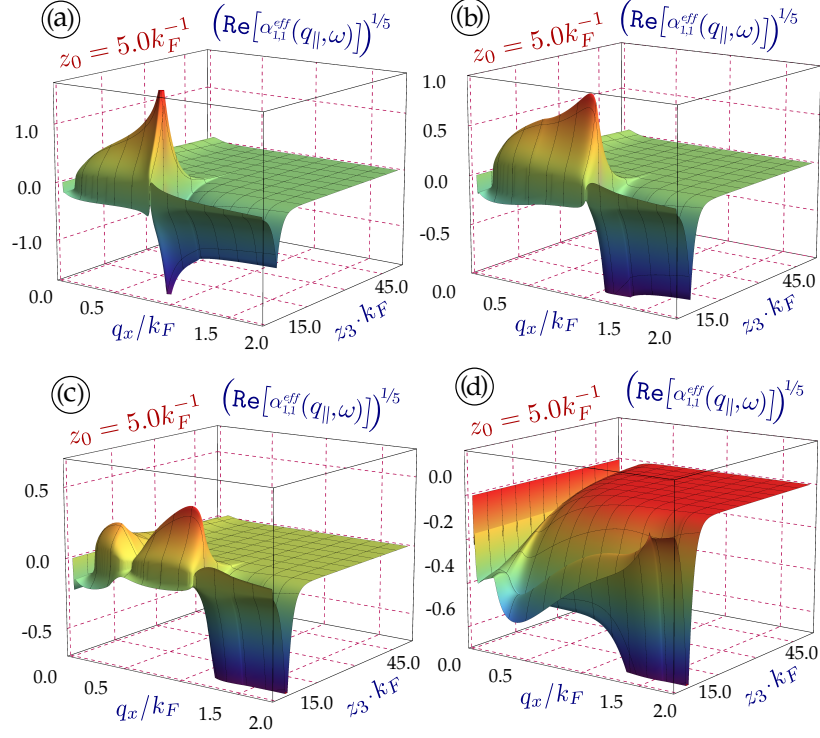


FIG. 5. 3D plots for  $[\text{Re}\{\alpha_{11}^{\text{eff}}(q_x, \omega|x_3)\}]^{1/5}$  with  $\omega/\Omega_r = 0.7$  (a),  $0.8$  (b),  $0.9$  (c),  $1.0$  (d), where  $k_F z_0 = 5$ ,  $\hbar\Omega_r/E_F = 1.78$ .

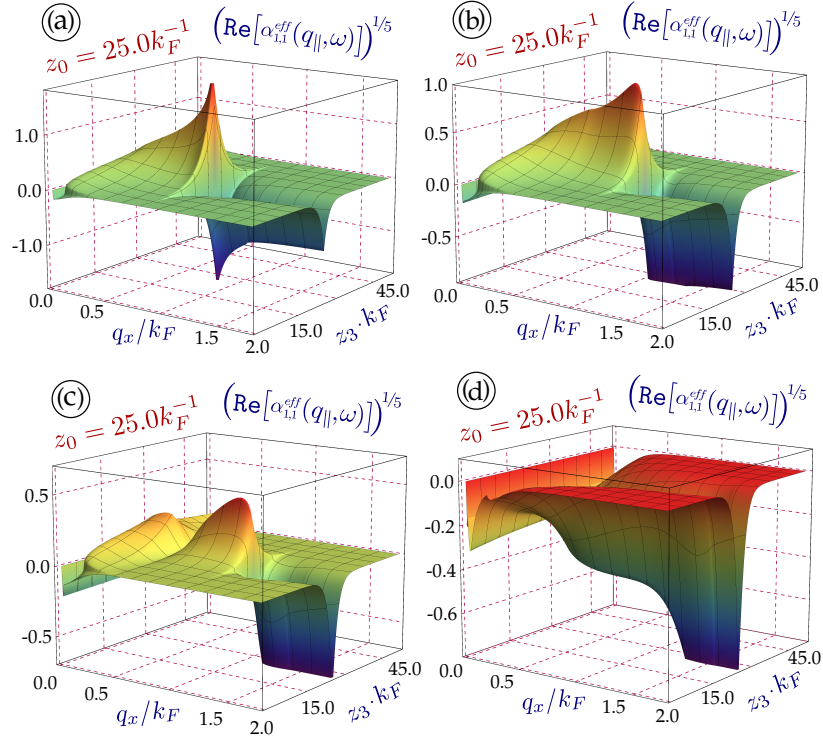


FIG. 6. 3D plots for  $[\text{Re}\{\alpha_{11}^{\text{eff}}(q_x, \omega|x_3)\}]^{1/5}$  with  $\omega/\Omega_r = 0.7$  (a),  $0.8$  (b),  $0.9$  (c),  $1.0$  (d), where  $k_F z_0 = 25$ ,  $\hbar\Omega_r/E_F = 1.78$ .